An Interaction-Admittance Model for Multi-Inverter Grid-Connected Systems

Minghui Lu, *Member, IEEE*, Yongheng Yang, *Senior Member, IEEE*, Brian Johnson, *Member, IEEE*, and Frede Blaabjerg, *Fellow, IEEE*

***Abstract*—In modern power systems, the increasing penetration of renewables and power electronics, particularly inverter-based wind and solar power generation, is altering power system dynamics and bringing new stability concerns. One challenging issue that is attracting considerable attention is the wide range of power oscillations associated with multiple parallel grid-connected inverters. In such systems, the characteristics in terms of resonance and oscillation are significantly different from single-inverter systems. This paper investigates the mutual interaction and stability issues of multiple grid-interfacing inverters with *LCL*-filters in power-electronics-based power systems under various grid conditions. The investigation reveals that such interactions between power inverters and the grid may excite multiple resonances at various frequencies under certain grid conditions. The nodal admittance matrix concept, which was originally from power systems engineering, is adopted here. Moreover, this paper further develops an Interaction-Admittance model that can effectively describe these mutual interactions in terms of a physical network admittance. We apply our model to various scenarios such as stiff grid conditions and inductive grids with/without power factor correction capacitors. The results with the proposed framework demonstrate an intuitive interpretation of multi-inverter system resonance and instabilities. Finally, simulations and experiments on a lab-scale system are provided to verify the theoretical analysis.**

***Index Terms*—Interaction admittance, multi-inverter system, resonance characteristics, stability analysis.**

I. Introduction

POWER systems have historically been constructed with large fossil-fuel-based generators with significant rotating mass or mechanical inertia. The collective inertia enables systems to absorb fluctuations and oscillations in load and generation [1]. The increasing penetration of renewable energy generation into the modern power system, such as solar farms and wind power plants, efficiently reduces the total consumption of fossil fuels [2]–[5]. It is reported that, by the end of 2015, more than 40% of the energy supply in Denmark was from wind power, and this number is expected to exceed 50% in near future (by 2020). By 2050, the plan is to be 100% free of fossil fuels and the wind energy will share a major part of the sustainable energy mix in Denmark [6]. The rapid adoption of renewable energy systems is leading to a variety changes.

1) Numerous power-electronics-based systems have been or are going to be installed into modern power generation and transmission system [7].
2) Compared to traditional power systems, power-electronics-based power systems have lower mechanical and electrical inertia but more capacitive and inductive components in converter filters and cables, making the power network more likely to be resonant and/or oscillatory [8].
3) More volatile system dynamics may be observed on low system inertia. In this context, the potential for stability and power quality issues are drawing increasing attention.

Grid-connected inverters act as the ubiquitous interfaces that are able to flexibly and efficiently connect the renewables to the grid. For instance, dozens or even hundreds of inverters are used in residential photovoltaics (PV) systems [9] and commercial wind power plant systems [10]. They may be connected in parallel to the low-voltage grid directly or in some applications via isolation transformers or to the medium-voltage (MV) grid via step-up transformers in large-scale renewable energy applications. In practice, to scale up the total generation capacity, grid-connected inverters usually operate in parallel. Recent works show that parallel inverters exhibit networked interactions in weak grids due to larger impedances. Results in [11] show that the equivalent grid impedance seen from a single inverter will be amplified by a factor of N when N identical inverters are connected at the point of common coupling (PCC). This analysis explains why the parallel system can still become unstable even if all the inverters meet the specifications at the individual level. The parallel operation significantly aggravates the overall network resonance and stability problems, which hinder the deployment of large-scale renewable plants.

Some interesting research works have been focusing on the interaction and coupling between grid-connected inverters [8], [9], [11]–[17]. Harmonic interactions have been observed [9] in a residential PV-distributed network containing large numbers of inverters in close proximity. A simplified passive model was presented to investigate the resonances, including

Manuscript received June 6, 2018; revised September 7, 2018; accepted October 25, 2018. Date of publication November 14, 2018; date of current version May 22, 2019. This work was supported by THE VELUX FOUNDATIONS under the VILLUM Investigator Grant—REPEPS (Award 00016591). Recommended for publication by Associate Editor L. Zhang. *(Corresponding author: Minghui Lu.)*

M. Lu and B. Johnson are with the Department of Electrical and Computer Engineering, University of Washington, Seattle, WA 98195 USA (e-mail: mhlu@uw.edu; brianbj@uw.edu).

Y. Yang and F. Blaabjerg are with the Department of Energy Technology, Aalborg University, Aalborg 9220, Denmark (e-mail: yoy@et.aau.dk; fbl@et.aau.dk).

Color versions of one or more of the figures in this paper are available online at http://ieeexplore.ieee.org.

Digital Object Identifier 10.1109/TPEL.2018.2881139

parallel resonance and series resonance without considering the contribution of inverter controllers. The method in [8] develops a useful resonance interaction model to analyze the multi-inverter system, where the current was divided into an interactive current that circulates among the converters and a common current that flows to the grid. Based on this model, the interactions and stability properties of different types of grid-connected inverters are examined [12]. Furthermore, it has been demonstrated in [13] that the interactive current can induce instability of multiple *LCL*-filtered inverters under the asynchronous pulsewidth modulation (PWM) carriers. Resonances at the *LCL*-filter resonance frequency are detected and observed in the individual inverter output current, but not in the grid current. Similarly, the harmonics from PWM are different from one inverter to another, which may trigger sideband harmonic resonances among the paralleled inverters. Under asynchronous carrier condition, the sideband resonances among parallel inverters will be triggered and then the interactive current becomes unstable [14]. Recently, the impedance-based stability analysis using the Nyquist criterion, first presented in [15], becomes an effective and popular alternative to study the stability and coupling of multiple-converter systems. For instance, the multiple-resonance problem in an inverter-based microgrid was investigated in [16], where the individual inverter was modeled as a Norton equivalent circuit: a current source in parallel with the output admittance. This method helps us to design an adaptive active damper to improve the stability of grid-connected inverters under weak grid, the damper emulates a resistor to damp the resonance between the grid-connected inverter and the grid [17].

The concept of passivity, originated from control theory and engineering [18], has recently been gaining attention [19]–[21]. It was adopted to design the converter current controller to mitigate harmonic interactions between parallel inverter units [19]. This concept can deal with a large and complex control system by imposing specific requirements for each individual subsystem to guarantee the overall system stability. Its basic idea is a phase-angle-based design for all connected subsystems, e.g., each subsystem should have a phase angle between $[-90°, +90°]$. Furthermore, the harmonic resonance for multiple grid-connected inverters based on the passivity theory was assessed in [20]. To guarantee the passivity of a renewable-energy-based power system, a method to cancel the negative real parts was proposed in [21]. In addition, component connection method has been adopted in [22] to analyze the stability of inverter-fed power systems.

In power engineering, the nodal admittance matrix (or just admittance matrix) or Y matrix or Y bus is an $N \times N$ matrix describing a power system with N buses [23], [24]. It represents the nodal admittance of the buses in a power system. The Y matrix is also one type of the required data to formulate a power flow study. In this paper, the nodal admittance matrix analysis is adopted to analyze the resonance and stability issues of multiple parallel grid inverters. Here, each inverter unit is regarded as an electrical node, and the multiple-input and multiple-output (MIMO) matrix is regards as the nodal admittance matrix. As a consequence, an interaction-admittance-based modeling method is proposed. Using this approach, the connection and interactions of these inverters can be directly identified by the characteristics of the interaction admittance.

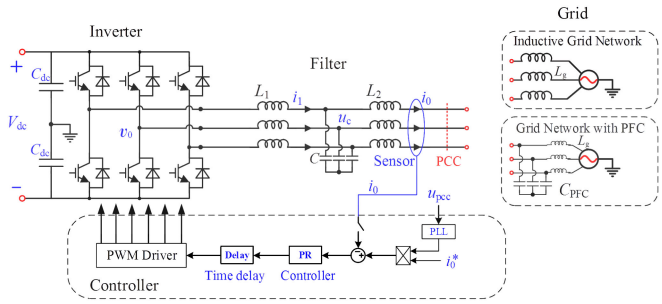

Fig. 1. Hardware schematic and the general control structure of an *LCL*-filtered grid-connected inverter.

Detailed modeling and interaction analysis under both the open-loop and closed-loop control are presented, beginning with an overall system description and modeling in Section II. Section III then introduces the nodal admittance matrix concept and the π-equivalent circuit. The concept of interaction admittance is also presented in Section III, which is evaluated under different grid conditions. Following, Section IV discusses the system stability considering the control scheme through the root locus analysis, where the contribution of controller is equivalent to a control impedance. Simulation and experimental results are provided in Sections V and VI, respectively, before the conclusion.

II. Modeling of the *LCL*-Filtered Grid-Interfacing Inverters

In this study, the current control implementation in the stationary reference frame (the α-β frame) is assumed here. Therefore, the conclusions investigated are applicable not only to single-phase systems, but also to per-phase control of multiphase systems. In this section, a single inverter and multiple parallel inverters are described and modeled.

A. System Description

Fig. 1 shows a typical three-phase voltage source inverter (VSI) connected to the power grid through an *LCL*-filter consisting of an inverter-side inductor L_1, a filter capacitor C, and a grid-side inductor L_2. No passive damping is considered as a worst case undamped scenario [25], [26]. The VSI achieves energy conversion between renewables and power grid. As shown in the figure, grid condition varies with the passive component at the grid side: 1) an inductive grid network: grid inductor in series with ideal grid voltage, 2) grid network with power factor corrector (PFC): a reactive compensation capacitor is taken into account, making the grid condition more complicated. The current loop regulates the current injected into the grid to guarantee a satisfactory power quality. Either the inverter-side current $i1$ or the grid-side current $i0$ of the *LCL*-filter can be chosen as a feedback variable. Phase-lock loop (PLL) is adopted to synchronize the grid voltage, in this paper, PLL is designed to be decoupled with inner control loops. A proportional resonant (PR) controller [27] can be adopted to further eliminate the steady-state current

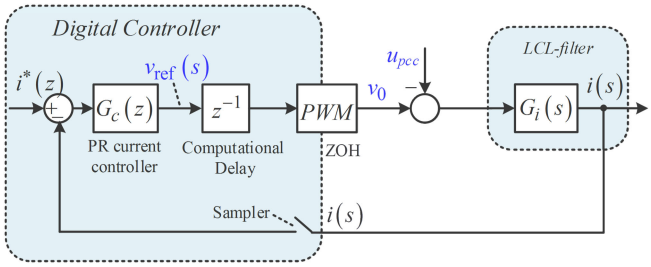

Fig. 2. Implementation of the digital controller in an *LCL*-filtered converter.

tracking error at the fundamental frequency. The PR controller is given as

$$G_c(s) = K_p + \frac{K_i \cdot s}{s^2 + \omega_0^2} \tag{1}$$

where ω_0 is the fundamental angular frequency, K_p is the proportional gain, and K_i is the resonant gain.

The control system is digitally implemented as shown in Fig. 2, where the sampling is synchronized with the converter switching carriers. The PWM process is assumed to operate within the linear range limited by the dc-link voltage [28]. *LCL*-filter has been modeled in the *s*-domain and the digital controller has been notated in the *z*-domain. Between the *LCL*-filter and digital controller are the sampler and pulsewidth modulator, which together with the non-zero computational time will introduce a total delay of approximately 1.5 times the sampling period T_s [29], [30]. A pure time delay in the digital controller can be expressed as

$$G_d(s) = e^{-1.5sT_s}. \tag{2}$$

Next, the system plant can be obtained where the transfer function $G_i(s)$ for relating the converter output voltage v_0 to the grid current i_0, as shown in Fig. 2, can be derived as

$$G_i(s) = \frac{i_0(s)}{v_0(s)} = \frac{1}{sL_1(L_2 + L_g)C} \frac{1}{s^2 + \omega_r^2} \tag{3}$$

where ω_r is the *LCL*-filter resonance frequency expressed as

$$\omega_r = \sqrt{\frac{L_1 + L_2 + L_g}{L_1(L_2 + L_g)C}}. \tag{4}$$

In (3), compared to the *L*-filtered system, a resonant part is undesirably introduced in the *LCL*-filtered system, which may make the system oscillatory, even unstable. Another observation from Fig. 1 is that there are two different grid conditions. One is the inductive grid network, where L_g represents the grid inductance including the transformer leakage inductance and transmission cable inductance, in some cases, varying within a large range. The situation is particularly critical in rural areas, where many distributed generation plants are connected [31]. The other grid condition considers a reactive power compensation unit at the PCC, helping to correct the entire system power factor such as the Static Compensator. An equivalent PFC capacitor $C_{\rm PFC}$ is added at the PCC in Fig. 1. The impact of this capacitance on the system stability and resonance will be discussed later.

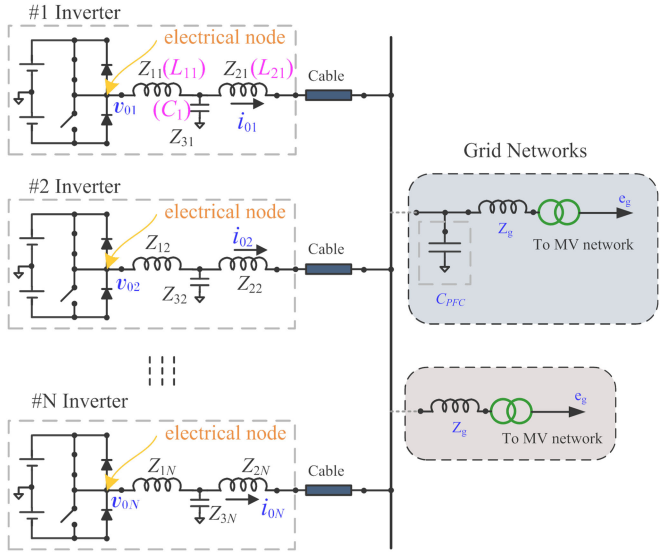

Fig. 3. Parallel operation of multiple grid-connected inverters to MV network.

B. Admittance Matrix Modeling and Analysis for Parallel Inverters

Fig. 3 shows an overall diagram consisting of multiple (number: *N*) above-described grid-interfacing inverters connected to the PCC. Z_{1i} and $Z_{2i}(i = 1, \ldots, N)$ are the inverter-side and grid-side inductor impedances, Z_{3i} are the filter capacitor impedances, Z_g is the grid impedance, and $C_{\rm PFC}$ is the PFC capacitor. They can be expressed as

$$Z_{1i} = sL_{1i},\ Z_{2i} = sL_{2i},\ Z_{3i} = \frac{1}{sC_i},\ Z_g = sL_g \tag{5}$$

where L_{1i} and L_{2i} are the inverter-side and grid-side inductors, and C_i is the filter capacitor of the *LCL*-filter for #*i* inverter.

As shown in Fig. 3, the inverter mid-points can be regarded as *electrical nodes*, the inverter output voltages v_{0i} are the voltages of these electrical nodes; i_{0i} are the grid-side inductor currents; the term e_g is the ideal and balanced grid voltage. In a stiff grid network, the grid impedance Z_g is considered to be zero. All the output currents i_{0i} flow to the grid. However, due to the existence of grid impedance, these parallel inverters are coupled with each other [11], meaning that one inverter's output behavior may influence the other inverters' performance. The dynamics of multiple parallel inverters shown in Fig. 3 can be expressed using the multivariable theory as

$$\mathbf{I}(s) = Y(s) \cdot \mathbf{U}(s) + S(s) \cdot e_g \Leftrightarrow$$

$$\begin{pmatrix} i_{01} \\ i_{02} \\ \cdots \\ i_{0N} \end{pmatrix} = \begin{pmatrix} Y_{11} & Y_{12} & \cdots & Y_{1N} \\ Y_{21} & Y_{22} & \cdots & Y_{2N} \\ \cdots & \cdots & \cdots & \cdots \\ Y_{N1} & Y_{N2} & \cdots & Y_{NN} \end{pmatrix} \cdot \begin{pmatrix} v_{01} \\ v_{02} \\ \cdots \\ v_{0N} \end{pmatrix} + \begin{pmatrix} S_1 \\ S_2 \\ \cdots \\ S_N \end{pmatrix} \cdot e_g \tag{6}$$

where the electrical node voltages $[v_{01},\ v_{02}, \ldots, v_{0N}]^{\rm T}$ are regarded as the input vector and the output currents $[i_{01},\ i_{02}, \ldots, i_{0N}]^{\rm T}$ are the output vector [32].

The $N \times N$ transfer matrix $\boldsymbol{Y}(s)$ is a system admittance matrix describing the influence of each electrical node voltage v_{0i} on the output current i_{0j}, $(i, j = 1, \ldots, N)$. $\boldsymbol{S}(s)$ characterizes the effect of the disturbance e_g on the output current i_{0i}. In this paper, only the current tracking reference is discussed. Noted that the influence analysis of the disturbance e_g can be found in [33] and [34]. Assume that all the installed inverters have identical parameters, then $Z_{1i} = Z_1 = sL_1$, $Z_{2i} = Z_2 = sL_2$, $Z_{3i} = Z_3 = 1/(\mathrm{sC})$. Each electrical node voltage v_{0i} has an identical impact on its own output current i_{0i}. Thus, the diagonals Y_{ii} are equal, i.e., $Y_{ii} = Y_{11}$; on the other hand, the non-diagonals Y_{ij} $(i \neq j)$ are also equal since each v_{0i} has the same effect on the otheri_{0j}, i.e., $Y_{ij} = Y_{12}$. Therefore, the admittance matrix $\boldsymbol{Y}(s)$ is a symmetric matrix, and Y_{11} and Y_{12} are obtained according to the circuit superposition principle as Eq. (7) and (8) shown at the bottom of this page.

The detailed derivation can be found in [35]. From (7) and (8), it is known that the element Y_{12} will be zero if the grid impedance Z_g is zero, and the transfer matrix $\boldsymbol{Y}(s)$ will be a diagonal matrix. It means that no mutual interactions appear in these inverters under a stiff grid condition. On the contrary, in an inductive grid [short-circuit ratio (SCR) is not infinite], the interactions will appear in the multiple parallel inverters due to the non-zero grid impedance Z_g. Notably, this situation is more realistic when the renewable penetration level increases.

C. Nodal Admittance Matrix

In power engineering, the nodal admittance matrix or *Y* matrix is an $N \times N$ matrix describing a power system with *N* buses, for instance, Fig. 4 presents a three-bus power system. It represents the nodal admittance of the buses in a power system. The term $y_k (k = 1, 2, 3)$ accounts for the admittance of linear loads connected to #*k* bus as well as the admittance-to-ground at #*k* bus, the term y_{ki} $(k \neq i)$ accounts for the admittance between two buses. The admittance matrix *Y* can be written as follows and typically a symmetric matrix as $y_{ki} = y_{ik}$.

As the theory above, the inverter mid-points can be regarded as electrical nodes/buses presented in Fig. 3, and the $\boldsymbol{Y}(s)$ in (6) can be regarded as a typical *nodal admittance matrix*. According to the definition given in [24], the diagonal elements Y_{ii} are called *self-admittances* at the nodes, illustrating the relationship between the node voltage $v_{0i}$and the corresponding output current with the same subscript i_{0i}; while the non-diagonals $Y_{ij(i\neq j)}$ are called *mutual-admittances*, describing the influence of the electrical node voltage v_{0i} on other output currents i_{0j}. This is applied to model and analyze the multiple inverters connected in parallel in this paper. The detailed analysis based on the nodal admittance matrix will be introduced to reveal the interactions and complex resonance characteristics of parallel inverters under different grid conditions in the following.

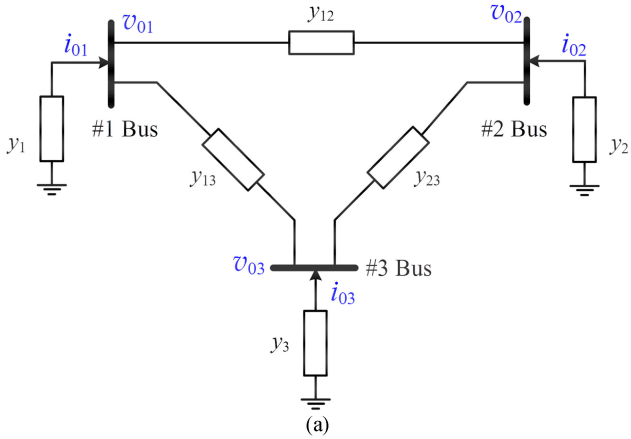

Fig. 4. Nodal admittance matrix. (a) The admittance diagram of a three-bus network. (b) The expression of admittance matrix *Y*.

III. Dynamic Interaction Analysis Based on the Interaction Admittance

A. Analysis of Two-Inverter System

The aim of this part is to analyze the dynamic interactions among these parallel inverters under different grid conditions using the *nodal admittance matrix* concept. For simplicity, this part begins with a two-inverter system, whose nodal admittance matrix is a second-order system and it can be written as

$$\begin{pmatrix} i_{01} \\ i_{02} \end{pmatrix} = \begin{pmatrix} Y_{11} & Y_{12} \\ Y_{21} & Y_{22} \end{pmatrix} \cdot \begin{pmatrix} v_{01} \\ v_{02} \end{pmatrix} \tag{9}$$

$$\begin{cases} i_{01} = Y_{11} \cdot v_{01} + Y_{12} \cdot v_{02} \\ i_{02} = Y_{21} \cdot v_{01} + Y_{22} \cdot v_{02} \end{cases} \tag{10}$$

which is an example of (6) with the inverter number $N = 2$. In (9), the diagonals Y_{11} and Y_{22} are the *self-admittances* and Y_{12} and Y_{21} are *mutual-admittances*, $Y_{11} = Y_{22}$ and $Y_{12} = Y_{21}$ due to the symmetrical characteristics. Fig. 5 shows the equivalent circuit of the two-inverter system admittance matrix, which includes a Norton impedance Y_{11} in parallel with a

$$Y_{ii} = \left.\frac{i_{0i}}{v_{0i}}\right| v_{0j} = 0, (j \neq i) = \frac{Z_3(Z_1Z_2 + Z_2Z_3 + Z_3Z_1)(Z_g + Z_c) + (n-1)Z_3Z_gZ_c(Z_1 + Z_3)}{(Z_1Z_2 + Z_2Z_3 + Z_3Z_1) \cdot ((Z_1Z_2 + Z_2Z_3 + Z_3Z_1) \cdot (Z_g + Z_c) + nZ_gZ_c(Z_1 + Z_3))} \tag{7}$$

$$Y_{ij(i\neq j)} = \left.\frac{i_{0i}}{v_{0j}}\right| v_{oj} \neq 0, (j \neq i) = \frac{Z_3Z_gZ_c(Z_1 + Z_3)}{(Z_1Z_2 + Z_2Z_3 + Z_3Z_1) \cdot ((Z_1Z_2 + Z_2Z_3 + Z_3Z_1) \cdot (Z_g + Z_c) + nZ_gZ_c(Z_1 + Z_3))}. \tag{8}$$

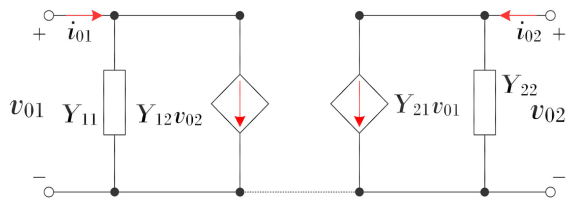

Fig. 5. Equivalent circuit with voltage-controlled current sources for the two-inverter system.

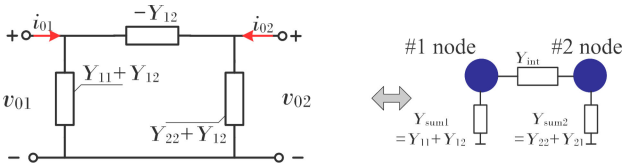

Fig. 6. π-equivalent circuit of parallel inverters.

voltage-controlled current source $Y_{12}\cdot v_{02}$. The current source represents the interactive effect between the parallel inverters.

In fact, the two voltage-controlled current sources $Y_{12}\cdot v_{02}$ and $Y_{21}\cdot v_{01}$ can be represented by a joint *impedance*. This can be achieved by transforming the circuit in Fig. 5 into a π-equivalent circuit for the two-inverter system, as shown in Fig. 6, in which the interactions among the inverters are replaced by a *physical admittance* $-Y_{12}$. The inverter #1 (node #1) and the inverter #2 (node #2) are connected through the joint admittance, which characterizes the interactions between the two parallel inverters. According to the transformation, the connection admittance equals to the negative Y_{12}, which is named *interaction admittance* Y_{int} as

$$Y_{\text{int}} = -Y_{12}. \tag{11}$$

The impedance between the electrical node #*i* to the ground is defined as Y_{sum_i}. In fact, it describes the interactions between the inverter module and the grid, which can be written as

$$Y_{\text{sum}\_i} = Y_{i1} + Y_{i2} + \cdots + Y_{ii} + \cdots + Y_{iN}. \tag{12}$$

Similarly, the same derivation can be done for the case where the inverter number N equals to 3, 4, 5, 6 and even more, as shown in Fig. 7. The interaction admittances indicate the connection of one inverter to all the remaining $(n-1)$ inverters, in which every two-inverter interaction can be expressed by the interaction admittance Y_{int}. Therefore, the interactions of the multi-parallel inverters system can be obtained by evaluating the characteristics of the *interaction admittance* Y_{int}.

To obtain a straightforward understanding on the interaction admittance Y_{int}, the diagonal and non-diagonal elements Y_{11} and Y_{12} can be rewritten as the equivalent equations given below

$$\begin{cases} \text{Diagonal } Y_{11} = \frac{N-1}{N} M_{LCL} + \frac{1}{N} M_{\text{Grid}} \\ \text{Non–Diagonal } Y_{12} = -\frac{1}{N} M_{LCL} + \frac{1}{N} M_{\text{Grid}} \end{cases} \tag{13}$$

$$\begin{cases} M_{LCL} = \frac{Z_3}{Z_1 Z_2 + Z_2 Z_3 + Z_3 Z_1} \\ M_{\text{Grid}} = \frac{Z_3}{(Z_2 + n Z_g)(Z_1 + Z_3) + Z_3 Z_1} \end{cases} \tag{14}$$

where M_{LCL} is the impedance characteristic of the *LCL* filter and M_{LCL} correlates neither with the inverter number nor with the grid conditions, and M_{Grid} is the transfer function considering the grid impedance coupling effect

$$Y_{\text{int}} = -Y_{12} = \frac{1}{N} M_{LCL} - \frac{1}{N} M_{\text{Grid}}. \tag{15}$$

Obviously, the *interaction admittance* Y_{int} is a function of the *LCL*-filter parameters, inverter number *N*, and the grid impedance Z_g, meaning that the interactions between parallel inverters change with the power grid conditions. Based on the above analysis, the interactions under three different grid conditions are discussed. Other grid conditions can be analyzed in a similar way.

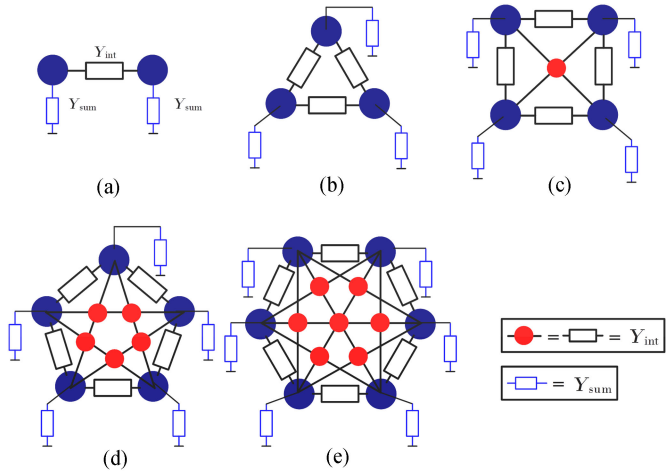

Fig. 7. Equivalent circuit of the node network for the inverter number. (a) $N = 2$. (b) $N = 3$. (c) $N = 4$. (d) $N = 5$. (e) $N = 6$.

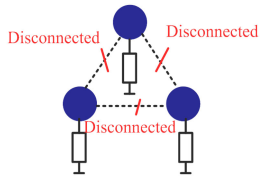

Fig. 8. Parallel inverters are equivalently disconnected with each other in the ideal stiff grid condition.

B. Ideal Stiff Grid

For a stiff grid condition, the grid impedance Z_g approaches to zero. According to (14), if $Z_g \approx 0$, $M_{LCL} \approx M_{\text{Grid}}$. Thus, the interaction admittance $Y_{\text{int}} \approx 0$, according to (15). There will be no mutual coupling effect among these inverters. These inverters are equivalently "disconnected" with each other, behaving like an individual inverter, as shown in Fig. 8. However, due to the complexity of the grid condition and existence of the grid impedance, one inverter can see not only the grid but also other inverters. Not all proportion of the inverter currents will be injected into the grid; instead, some portion of the currents will circulate in these parallel inverters through interactive admittances Y_{int}.

C. Inductive Grid Impedance

If the grid impedance Z_g is a non-zero value, an inductive grid condition is assumed in this paper. The magnitude and

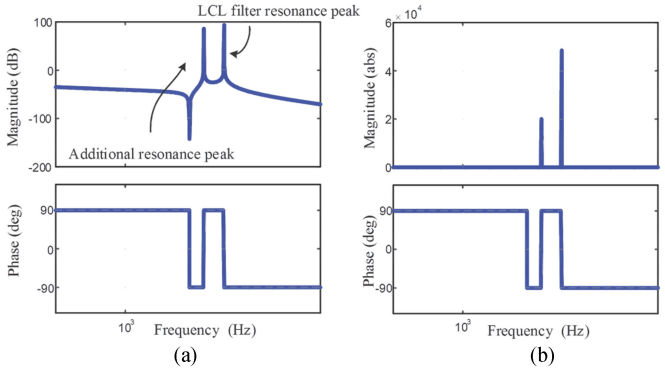

Fig. 9. Frequency characteristics of the interaction admittance of two inverters. (a) Magnitude unit: dB. (b) Absolute value.

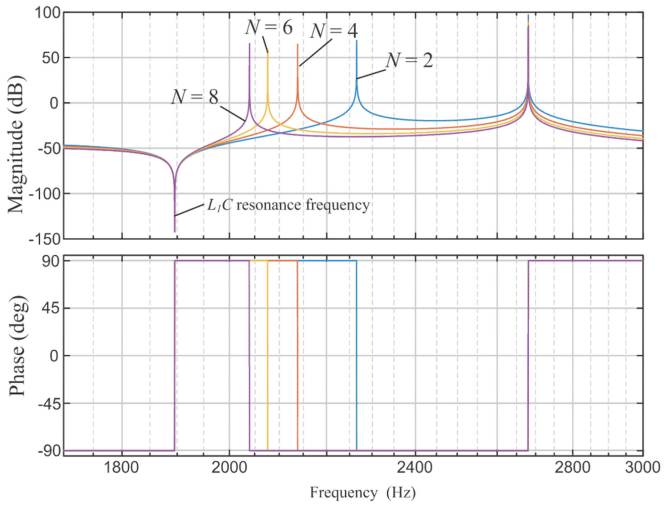

Fig. 10. Frequency characteristics of the interaction admittance with different inverter numbers.

phase characteristics of the two-inverter interaction admittance $Y_{\rm int}$ are shown in Fig. 9, from which two resonance peaks can be observed. Compared with the ideal grid condition, an additional resonance peak is introduced: one resonance frequency is equal to *LCL*-filter resonance frequency while the other is aroused by the interaction in the multi-inverter system. At both two resonance peaks, the interactive admittance $Y_{\rm int}$ is equal to an infinite value if without any damping. It implies that the current at these frequencies will be amplified. As a result, it is likely to excite the resonant currents at these two frequencies.

It is clear that the parallel operation of multiple grid-connected inverters significantly alters the magnitude and phase under the inductive grid impedance condition, as seen in Fig. 9. It should be noted that these two resonance frequencies change with the inverter numbers. Fig. 10 shows the magnitude responses of different inverter numbers ($N = 2, 4, 6, 8$). According to (14), one of the resonance peaks is fixed and equal to the *LCL*-filter resonance frequency, which is activated by the term M_{LCL}. The other resonance peak is caused by the term $M_{\rm Grid}$, and its resonance frequency decreases with inverter numbers because of $N{\cdot}Z_g$ in the denominator. If N is quite large, the frequency will decrease to the resonance frequency of L_1 and

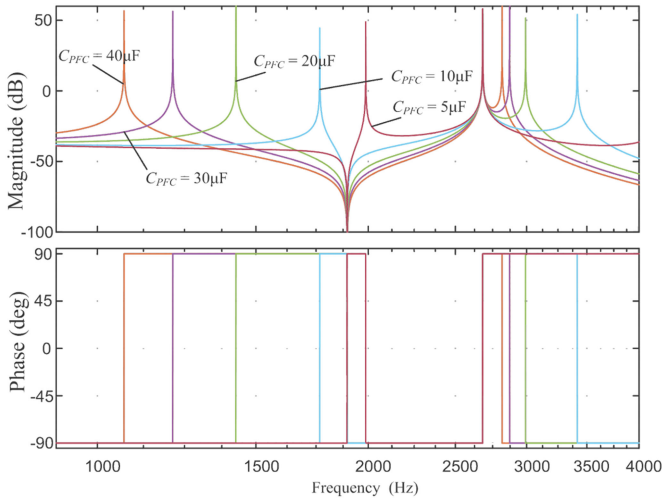

Fig. 11. Frequency characteristics of the parallel operation under the inductive grid with PFC capacitor.

capacitor C as

$$\omega_r = \sqrt{\frac{L_1 + L_2 + N \cdot L_g}{L_1(L_2 + N \cdot L_g)C}} \Rightarrow \omega_{r\_\lim} = \sqrt{\frac{1}{L_1 C}}. \quad (16)$$

As shown in Fig. 10, the lower resonant frequency decreases with the increase of the inverter number and approaches the limit frequency. The two resonance peaks situation complicates the controller design and stability analysis.

D. Inductive Grid Impedance With PFC Capacitor

In many grid-connected applications, passive PFC capacitors or active reactive power compensation units need to be installed and connected to the PCC for power factor correction, as stated in Section II. Their practical effects can be replaced by an equivalent passive capacitance $C_{\rm PFC}$. Its installation even complicates the resonance features of multiple inverters. Fig. 11 presents the frequency response of parallel inverters under the inductive grid with the PFC capacitor. It can be observed that the PFC capacitor increases the system resonance complexity. In addition to the two resonant peaks for the inductive grid condition, one more resonance peak is introduced to the grid-side current. That is, there are three resonant peaks: one resonance peak is fixed at the *LCL*-filter resonance frequency, another one locates above the *LCL* resonance frequency, and the last one is below the resonance frequency. In this case, the grid impedance Z_g in (13) and (14) can be replaced by

$$Z_g' = Z_g/(L_g \cdot C_{PFC} \cdot s^2 + 1). \quad (17)$$

It has been demonstrated that there is a limit for the lower resonance peak frequency under inductive grid condition. However, it is different in the case of the PFC capacitor, which can make the lower frequency even closer to the control bandwidth. The resonant feature may worsen the system stability and performance.

This section discusses the passive resonance characteristics of parallel inverters under different grid conditions. However, the

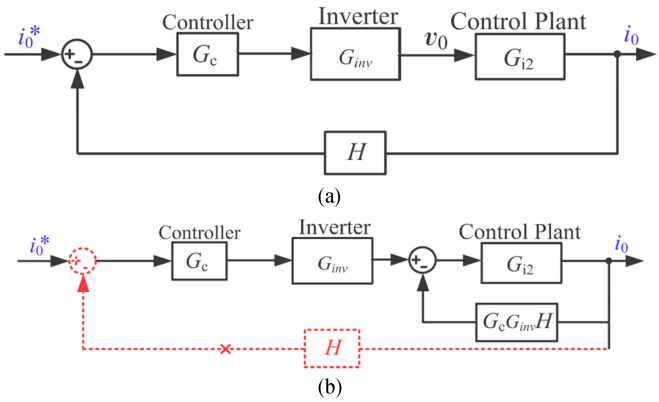

Fig. 12. Current control system. (a) The control structure diagram. (b) The equivalent control diagram.

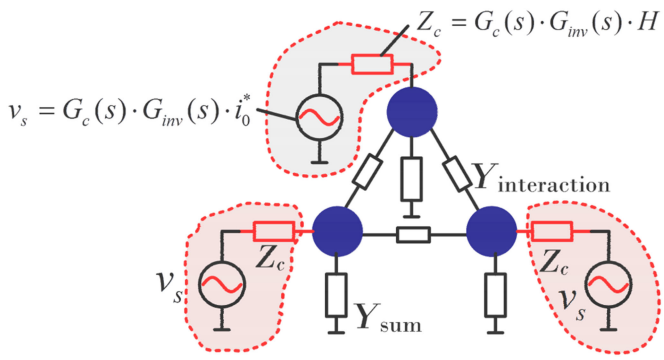

Fig. 13. Equivalent circuit of multi-parallel inverters considering the closed-loop control.

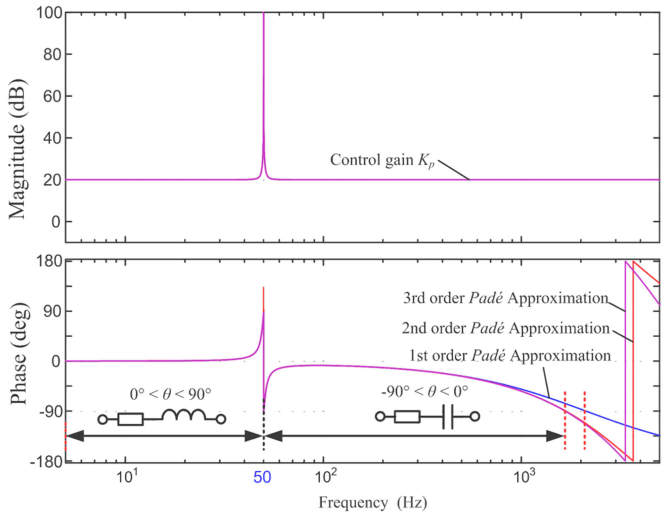

Fig. 14. Bode diagram and impedance equivalence of Z_c under different frequency ranges.

contribution of controller has not been taken into consideration. In Section IV, the impact of controller on the system stability of parallel inverters is discussed.

IV. Analysis of Current Controller Contribution to System Stability

This part will discuss the performance and system stability when the inverter current control scheme is involved. As mentioned in the previous section, the dynamics of the studied inverters are coupled due to the grid impedance. In this paper, the grid-side current is selected for the current control.

A. Model of the Closed-Loop Current Control

Stable operations of *LCL*-filtered inverters without any additional damping have been proved to be possible in [16] and [26]. Without loss of generality, a simple and effective single-loop control with a typical PR controller is chosen. The implemented inner current control scheme is shown in Fig. 12, where $G_c(s)$ is the controller transfer function, as shown in (1), $G_{\text{inv}}(s)$ is the inverter transfer function including the calculation delay and PWM delay, and $H(s)$ is the feedback coefficient. The total delay is considered as 1.5T s, as expressed in (2), and the *Padé* approximation can be adopted to approximate the time delay. As shown in Fig. 12(b), the feedback point is moved right after $G_{\text{inv}}(s)$, the feedback term is $G_c(s)\cdot G_{\text{inv}}(s)\cdot H$.

As shown in Fig. 13, the grid current closed-loop control can be modeled as one voltage source in series with one *control impedance* $Z_c = G_c(s)\ G_{\text{inv}}(s)\ H$. The inverter bridge output voltage can then be expressed as

$$v_{0i} = G_c(s)\cdot G_{\text{inv}}(s)\cdot i_{0i}^* - G_c(s)\cdot G_{\text{inv}}(s)\cdot H\cdot i_{0i}. \quad (18)$$

Fig. 14 shows the Bode diagram of the *control impedance* Z_c, where three *Padé* approximation methods are compared. Different frequency responses are observed at the high frequency range above 1 kHz, whereas quite similar responses at lower frequencies. From the phase feature, it can be seen that the control impedance Z_c is resistive-inductive in the range [0 Hz, 50 Hz], and is resistive-capacitive beyond 50 Hz. Therefore, the contribution of the current control to system stability can be replaced by the control impedance Z_c.

B. Mutual-Current and Self-Current

As mentioned previously, the parallel inverters are connected to each other through the *interaction admittance* Y_{int}, as shown in Fig. 7. If the interactions exist in the parallel inverters, there will be currents flowing through these interactions admittance; otherwise, there will be no interactions among these inverters. In this paper, the current through the interaction admittance is defined as *mutual-current*. When considering a system with *N* inverters, the current can be divided into *N* parts: *N*–1 mutual-currents flowing to other parallel inverters through interaction impedance; and the rest of the current flowing into the sum admittance $Y_{\text{sum\_1}} = Y_{11}+Y_{12}+\cdots+Y_{1N}$. The current on the sum admittance Y_{sum} is defined as *self-current*.

C. Dynamics and Stability Analysis of Multiple Parallel Inverters

As shown in Fig. 15, the mutual-current i_{m_ij} between the #*i* inverter and #*j* inverter and its self-current $i_{\text{self\_}i}$ can be

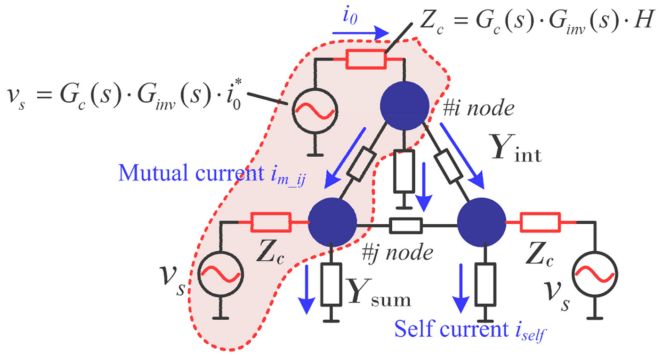

Fig. 15. Equivalent circuit of multi-parallel inverters considering the closed-loop control.

written as

$$i_{m\_ij} = (v_{0i} - v_{0j}) \cdot Y_{\text{int}} \tag{19}$$

$$i_{\text{self}\_i} = v_{0i} \cdot Y_{\text{sum}} \tag{20}$$

where v_{0i} and v_{0j} are the voltages at #*i* and #*j* node, respectively.

The relationship among the mutual-current i_{m_ij} and the self-current i_{self_i} and the output current i_{0_i} is expressed according to *Kirchhoff*'s current law as

$$i_{0\_i} = \sum_{j=1, j\neq i}^{N} i_{m\_ij} + i_{\text{self}\_i}. \tag{21}$$

Combining (18)–(21), the *mutual-current* and *self-current* can be derived as

$$i_{m\_ij} = \frac{G_c \cdot G_{\text{inv}} \cdot Y_{\text{int}}}{(1 + M_{LCL} \cdot Z_c)} \cdot (i_{0i}^* - i_{0j}^*), \quad i \neq j \tag{22}$$

$$i_{\text{self}\_i} = \sum_{j=1, j\neq i}^{N} \frac{1}{N} \cdot \frac{G_c \cdot G_{\text{inv}} \cdot Y_{\text{sum}}}{(1 + M_{LCL} \cdot Z_c)} \cdot (i_{0i}^* - i_{0j}^*) + \frac{1}{N} \cdot \frac{G_c \cdot G_{\text{inv}} \cdot Y_{\text{sum}}}{(1 + M_{\text{Grid}} \cdot Z_c)} \cdot (i_{01}^* + \cdots + i_{0n}^*) \tag{23}$$

which indicates that i_{m_ij} is a function of the interaction admittance Y_{int} and *control impedance* Z_c, while i_{self_i} is a function of the total admittance Y_{sum_i}. Substituting (22) and (23) into (21) yields the output current as (24) shown at the bottom of this page.

Merging the different current references in (24), the inverter output current can then be divided into two major terms: reference tracking characteristic transfer function $T(s)$ and other

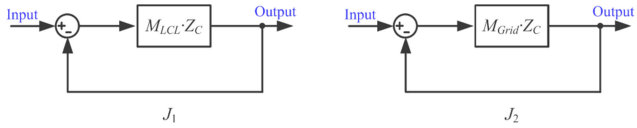

Fig. 16. Equivalent control block diagram of $J_1(s)$ and $J_2(s)$.

output current impact transfer function $R(s)$. $T(s)$ stands for the reference tracking characteristic while $R(s)$ stands for the influences from other inverters. They correspond to the concepts in the *classical control theory*: $T(s)$ resembles the complementary sensitivity function whereas $R(s)$ resembles sensitivity function [32]. $T(s) - R(s) = 1$. It implies that the #*i* output current i_{0_i} not only depends on its own current reference $i_{0\_i}^*$, but also it is affected by other output current references $i_{0\_j}^*$. Those can be expressed as

$$T(s) = \frac{n-1}{n} \cdot \frac{M_{LCL} \cdot Z_c}{(1 + M_{LCL} \cdot Z_c)} + \frac{1}{n} \cdot \frac{M_{\text{Grid}} \cdot Z_c}{(1 + M_{\text{Grid}} \cdot Z_c)} \tag{25}$$

$$R(s) = -\frac{1}{n} \cdot \frac{M_{LCL} \cdot Z_c}{(1 + M_{LCL} \cdot Z_c)} + \frac{1}{n} \cdot \frac{M_{\text{Grid}} \cdot Z_c}{(1 + M_{\text{Grid}} \cdot Z_c)}. \tag{26}$$

Both $T(s)$ and $R(s)$ contain the inverter number n, *control impedance* Z_c, and transfer functions M_{LCL} and M_{grid}. n is a symbol to replace the inverter number N in (24)–(26). They are the linear combinations of $J_1(s)$ and $J_2(s)$ that are written as

$$J_1(s) = \frac{M_{LCL} \cdot Z_c}{(1 + M_{LCL} \cdot Z_c)} \text{ and } J_2(s) = \frac{M_{\text{Grid}} \cdot Z_c}{(1 + M_{\text{Grid}} \cdot Z_c)} \tag{27}$$

where $J_1(s)$ and $J_2(s)$ are the closed-loop transfer functions of two single-input single-output feedback systems, as shown in Fig. 16. In fact, $J_1(s)$ describes the closed-loop model of the *LCL*-filtered inverter connected to the stiff grid. It is the function of M_{LCL} and *control impedance* Z_c. In contrast, $J_2(s)$ describes the closed-loop model of the inverter connected to the grid with $n \cdot Z_g$ grid impedance.

Fig. 17 plots the step responses of $J_1(s)$ and $J_2(s)$, which shows that they have quite different dynamics due to the difference between M_{LCL} and M_{grid} [see (14)]. Compared to M_{LCL}, M_{grid} has an additional term $n \cdot Z_g$ in the denominator. It means that the dynamic difference of $J_1(s)$ and $J_2(s)$ depends on the inverter number n and the grid impedance Z_g. In steady-state, both $J_1(s)$ and $J_2(s)$ are approaching unity.

$$i_{0\_i} = i_{\text{self}\_i} + \sum_{j-1, j\neq i}^{n} i_{m\_ij} = \sum_{j-1, j\neq i}^{n} \frac{1}{n} \cdot \frac{M_{LCL} \cdot Z_c}{(1 + M_{LCL} \cdot Z_c)} \cdot (i_{0i}^* - i_{0j}^*) + \frac{1}{n} \cdot \frac{M_{\text{Grid}} \cdot Z_c}{(1 + M_{\text{Grid}} \cdot Z_c)} \cdot (i_{01}^* + \cdots + i_{0n}^*)$$

$$= \underbrace{\left[\frac{n-1}{n} \cdot \frac{M_{LCL} \cdot Z_c}{(1 + M_{LCL} \cdot Z_c)} + \frac{1}{n} \cdot \frac{M_{\text{Grid}} \cdot Z_c}{(1 + M_{\text{Grid}} \cdot Z_c)}\right] \cdot i_{0i}^*}_{\text{Reference Tracking Characteristic } T(s)} + \underbrace{\sum_{j-1, j\neq i}^{n} \left[\frac{1}{n} \cdot \frac{M_{LCL} \cdot Z_c}{(1 + M_{LCL} \cdot Z_c)} + \frac{1}{n} \cdot \frac{M_{\text{Grid}} \cdot Z_c}{(1 + M_{\text{Grid}} \cdot Z_c)}\right] \cdot i_{0j}^*}_{\text{Output Current Reference Impact } R(s)} \tag{24}$$

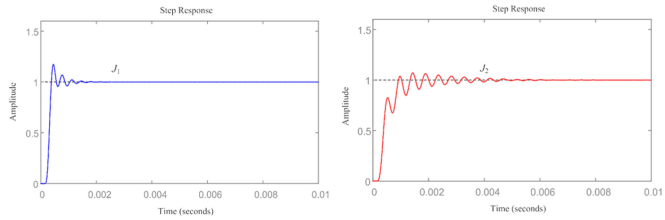

Fig. 17. Step responses of $J_1(s)$ and $J_2(s)$.

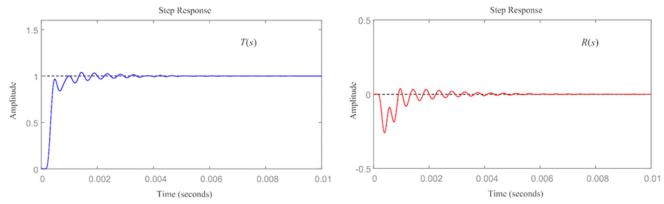

Fig. 18. Step responses of $T(s)$ and $R(s)$.

Moreover, the step responses of $T(s)$ and $R(s)$ are plotted in Fig. 18. Due to the impact of $J_2(s)$, the reference tracking transfer function $T(s)$ is equal to neither $J_1(s)$ nor $J_2(s)$, but their linear combinations. From the mathematic perspective, $T(s)$ will approach $J_1(s)$ when the inverter number n increases. It indicates that the influence of other modules on the inverter is the largest when the inverter number is 2. The other inverter impact transfer function $R(s)$ is approaching zero in the steady-state according to (26) because both $J_1(s)$ and $J_2(s)$ are approaching unity. It means that the other inverters have negligible impact on the steady-state behaviors, and they only affect the dynamic responses.

In order to explore the stability of multiple parallel inverters with *LCL*-filters, the entire system stability is classified as *Reference Tracking T(s) stability* and *Impact Transfer Function R(s) stability*. $T(s)$ and $R(s)$ are linear combinations of $J_1(s)$ and $J_2(s)$, and consequently, the whole system stability is transformed into the stability of $J_1(s)$ and $J_2(s)$. If any of $J_1(s)$ and $J_2(s)$ is unstable, the impact transfer function *R(s)* will diverge, and the system becomes unstable. The detailed example and application will be discussed in the following.

V. Simulation Analysis and Results

Simulations are performed on the co-simulation platform of MATLAB/Simulink and PLECS, where the main circuit topology is built in PLECS and the control scheme is executed in MATLAB. The controller is constructed in the discrete domain. The simulation model includes three-phase grid-connected inverters with *LCL*-filters, as well as the grid impedance/inductance and PFC capacitors describing the grid conditions. The inverter number is three. Table I lists the system parameters of simulation model.

A. Ideal Stiff Grid Condition

In the stiff grid case, the grid inductance L_g is equal to zero, $L_g = 0\,\text{mH}$. According to (14) and (15), $M_{LCL} = M_{\text{grid}}$, the interaction admittance $Y_{\text{int}} = 0$, meaning that there will be no admittance allowing the mutual-current to pass through.

TABLE I
Simulation Model Parameters

Nominal System Parameters		
Power Rating	S	15 kW
Grid frequency	f_g	50 Hz
DC-link voltage	V_{dc}	730 V
Grid voltage	V_g	380 Vrms
Sampling frequency	f_s	10 kHz
Switch frequency	f_{sw}	10 kHz
Parameters of grid-connected inverter		
Converter-side inductor	L_1	1.5 mH
Filter capacitor	C_f	4.7 μF
Grid-side inductor	L_2	1 mH
Resonance frequency	f_r	2.51 kHz
Parameters of grid condition		
Grid inductance	L_g	0.8 mH
Filter capacitor	C_f	7 μF

Furthermore, as (25)–(27), $J_1(s) = J_2(s)$, the reference tracking $T(s) = J_1(s)$, while the impacts from remaining inverters $R(s) = 0$. It means that other inverters have no impact on the output characteristic of the inverter output current. The parallel units are operating individually as a single inverter in an ideal grid condition, which has been well known. Fig. 19 shows the performance of three parallel inverters in the ideal stiff grid. It shows the individual inverter system bandwidth is designed at 820 Hz, and all the system poles are located inside the unit circle. At $t = 0.165$ s, a step change from 10 to 15 A in the #1 inverter current reference is set to observe the dynamics, the result verifies the system stable operation during transient process. Three inverters are operating in good condition to inject power into the power grid.

Fig. 20 shows the simulation results of another case. As analyzed, the inverters will have no impact on other inverters due to the zero *interaction admittance*. Here, the #1 inverter becomes unstable through adjusting the control gain out of the stable boundary; it can be observed that other inverters are still stable. The unstable operation of #1 inverter does not influence other inverters.

B. Inductive Grid Condition

In the real grid condition, the grid impedance exists in the grid networks in a big or little number due to the physical elements, such as long transmission cables and transformers. The grid strength is numerically reflected by a term SCR, a ratio between the grid short-circuit power and inverter nominal power. A larger SCR means a stronger ac grid while as a smaller SCR leads to a weak grid. Due to the grid impedance, the increasing

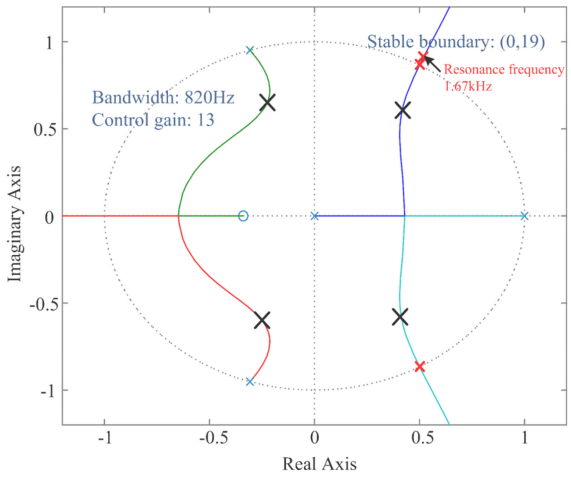

(a)

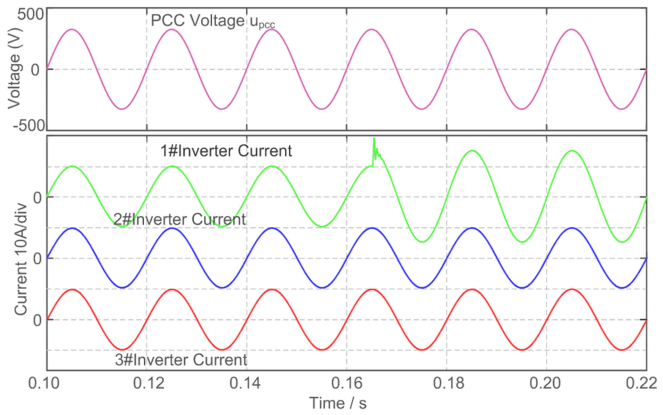

(b)

Fig. 19. Grid-connected inverters operating in the ideal stiff grid condition. (a) The stable operating point of inverters with bandwidth 820 Hz and control gain 13. (b) Simulation results of multiple inverters system for a stable case.

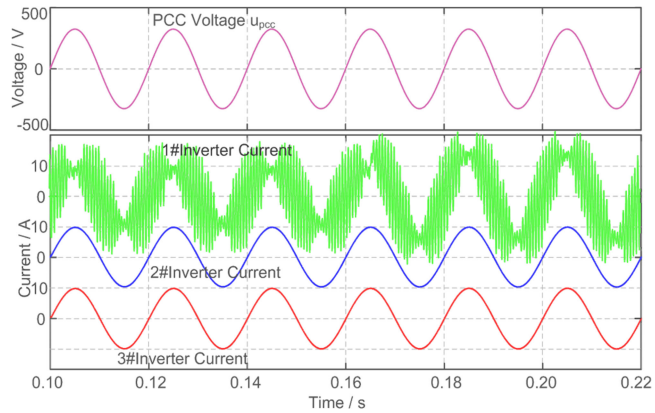

Fig. 20. Simulation results of multiple inverters, where the #1 inverter is unstable and the other two inverters are stable.

total inductance L results in a larger control gain limit (the stable boundary changes from 19 to 22.8) and a smaller bandwidth 520 Hz (830 to 520 Hz). The stability of multiple-inverter system is divided into $J_1(s)$ stability and $J_2(s)$ stability. For $J_1(s)$ stability, it only depends on the filter parameters and controller parameters, it has been shown in Fig. 19(a). Compared to $J_1(s)$,

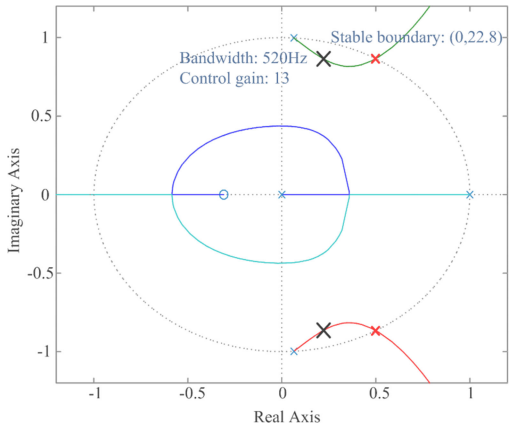

Fig. 21. Root locus of $J_2(s)$ under an inductive grid condition.

$J_2(s)$ is different due to the additional impedance $n \cdot Z_g$. Hence, the stability status of $J_2(s)$ also varies from $J_1(s)$. For instance, Fig. 21 presents the stable operating point of $J_2(s)$ with three parallel inverters ($n = 3$) and grid impedance $Z_g = 0.5$ mH provided that the inverter controller and filter parameters are kept the same. It can be observed that stable boundary is larger and the bandwidth of $J_2(s)$ changes from 820 Hz [the bandwidth of $J_1(s)$] to 520 Hz.

As for the different stable boundaries and bandwidths for $J_1(s)$ and $J_2(s)$, if the bandwidth and control gain are within the boundaries of $J_1(s)$ and $J_2(s)$, then the entire system is stable. On the other hand, if the control gain exceeds the boundaries of $J_1(s)$ and $J_2(s)$, the entire system will become unstable. In addition, it is still likely to have the case that $J_2(s)$ is stable while $J_1(s)$ is unstable because $J_2(s)$ has a wider stable boundary than $J_1(s)$ due to the larger inductor for $J_2(s)$. Fig. 22 presents the case that the #1 inverter and #2 inverter are unstable while the #3 inverter is stable. The control gain for these inverters are: #1, $K_{p1} = 21$; #2, $K_{p2} = 21$; and #3, $K_{p3} = 13$. There are resonant currents circulating between #1 inverter and #2 inverter, and the mutual-current is unstable. The resonance frequency can be identified on the root locus plot, which is around 1.67 kHz. This analysis above is in agreement with the outcome presented in [8].

Fig. 23 shows the case where the control gains of all the three inverters are equal to 21. It can be observed that the currents are circulating among these three inverters. However, the sum of the three currents is still sinusoidal. Different from the traditional concept of circulating current, the resonant mutual-currents only circulate among the ac side, and the dc-link voltage remains stable during the operation. Fig. 24 shows the simulation results of the dc-link voltage.

C. Inductive Grid Condition With Power Factor Correction Capacitor

If the PFC capacitor C_{PFC} is taken into consideration in parallel-inverter system, the analysis will be more complicated because the additional capacitor increases the system order. Notably, through the theory proposed in this paper, system stability in such situation still can be classified into two stability conditions: $J_1(s)$ stability and $J_2(s)$ stability. For $J_1(s)$ stability, it is the

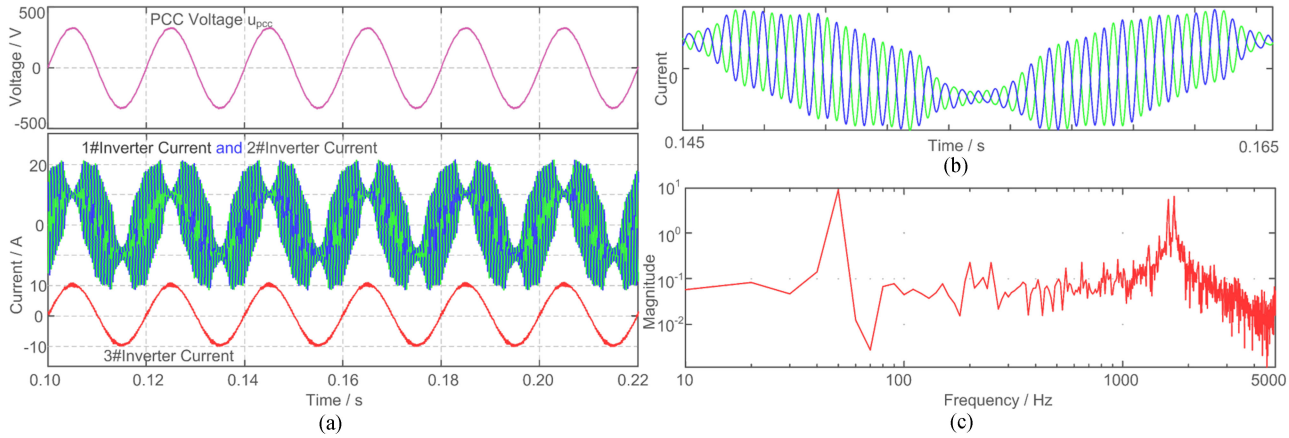

Fig. 22. Simulation results of three inverters operating in an inductive grid, two inverters are unstable. (a) PCC voltage and output currents. (b) Zoom in 1# and 2# currents. (c) Magnitude response.

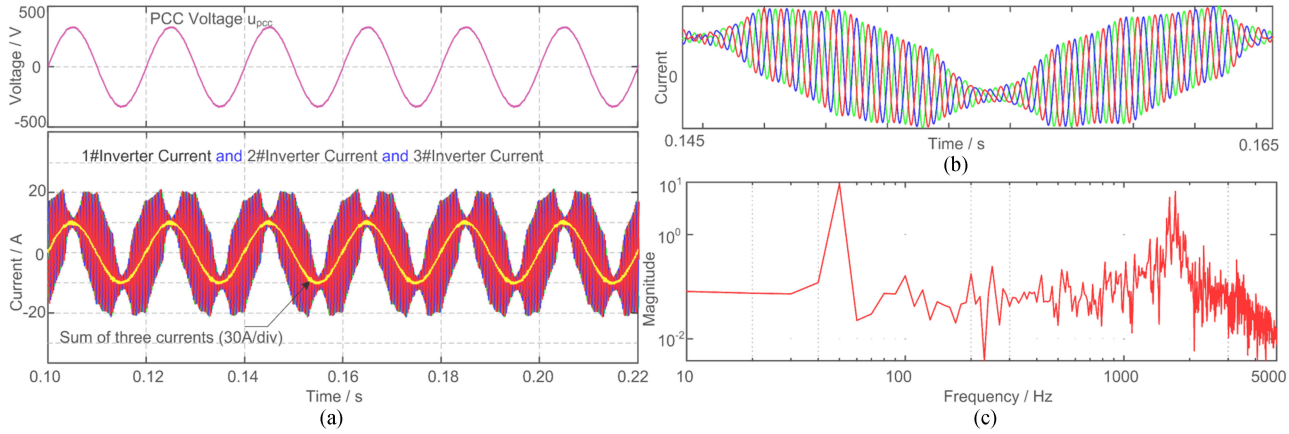

Fig. 23. Simulation results of three inverters operating in an inductive grid, three inverters are unstable. (a) PCC voltage and output currents. (b) Zoom in 1#, 2#, and 3# currents. (c) Magnitude response.

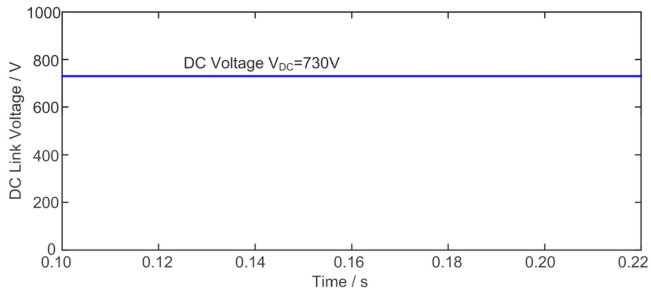

Fig. 24. Simulation results (the dc-link voltage) of the multiple-inverter system under an inductive grid condition.

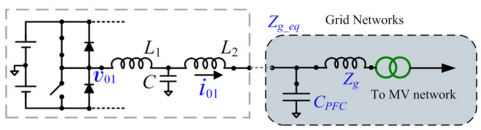

Fig. 25. Equivalent circuit for $J_2(s)$ if the PFC capacitor C_{PFC} is added.

same with previous analysis. For $J_2(s)$ under this grid condition, the inverter-grid system has been changed, as shown in Fig. 25. It is a *five-order* system with an equivalent grid impedance Z_{g_eq} that can be expressed as

$$Z_{g\_\mathrm{eq}} = n \cdot \left(Z_g \parallel Z_{\mathrm{PFC}}\right) = \frac{n \cdot L_g s}{L_g C_{\mathrm{PFC}} s^2 + 1}. \tag{28}$$

As shown in (28), the grid impedance Z_{g_eq} is equal to zero if the grid series inductance L_g is equal to zero, and then the PFC capacitor has no influence on the system stability. It implies that PFC capacitor has no impact on system stability alone without grid inductance. Therefore, the following analysis concentrates on the scenarios where the grid inductance L_g is a non-zero value. Fig. 26 plots the root locus of $J_2(s)$ under an inductive grid condition with PFC capacitor C_{PFC}. Compared to the previous root loci in Figs. 19 and 21, two more poles (six poles in total) and two more zeros (on the circle edge) are introduced, and therefore, the stability status of multiple inverters is altered. By plotting different root loci, it can be concluded the additional zeros are induced by the resonant part of grid impedance L_g and PFC capacitor C_{PFC}. So, the root locus changes with the variation of L_g and C_{PFC}.

To clarify the influence of the grid inductance L_g on the system stability, four sets of grid conditions in Table II are compared while the PFC capacitor is a fixed at $C_{\mathrm{PFC}} = 40\ \mu$F.

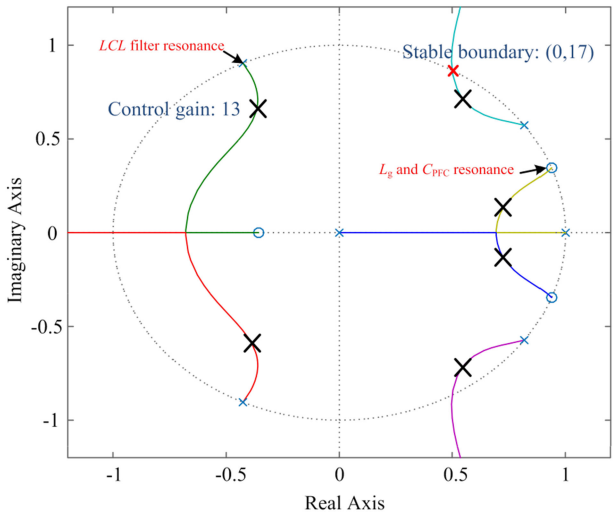

Fig. 26. Root locus of $J_2(s)$ under an inductive grid condition with PFC capacitors C_{PFC}.

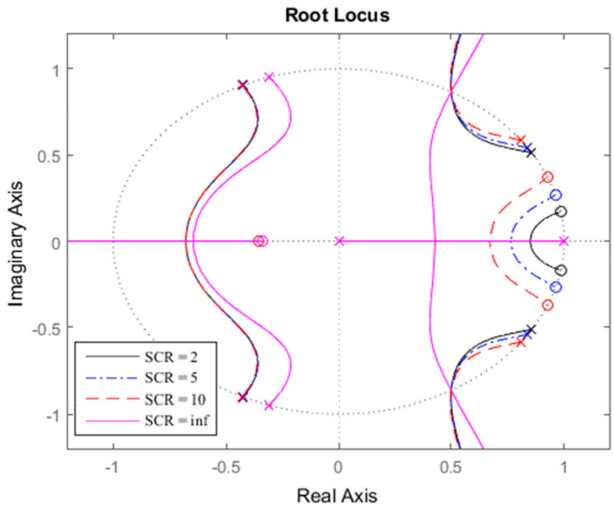

Fig. 27. Root loci for different SCR and grid conditions.

The results are shown in Fig. 27. It can be observed that the root locus is the same with a single inverter as Fig. 19(a) when the grid is stiff (SCR $= \infty$). With the increase of the grid inductance L_g or decrease of the SCR value, two zeros induced by L_g and C_{PFC} become closer to the (1,0) point. It is interesting to note that all the root loci crossover the point (1/2, $\pm\sqrt{3}/2$) and the stable regions of different SCR values are similar to each other.

Fig. 28 presents the stable regions with various PFC capacitances: (a) plots the root loci with relatively large capacitance from 10 to 100 μF and (b) plots the root loci when the PFC capacitance ranges from 1 to 5 μF. The grid inductance L_g is chosen as #3 condition in Table II, $L_g = 3.4\,\mathrm{mH}$ (SCR $= 5$). From the figures, these root loci are quite different from each other if the PFC capacitances are selected in different ranges. It can be observed that the system with the 100 μF PFC capacitor has a wider stable region than the system with 10 μF. The reason is that the PFC capacitor offers grid voltage support at the PCC, and then the negative influence of the grid impedance Z_g will be lessened. On the other hand, the PFC capacitor also brings resonance to the system. Fig. 28(b) reveals that a relatively small capacitor will bring two resonant poles outside the unit circle, meaning that the system will turn to unstable no matter what the control gain is.

Fig. 29 presents the simulation results comparing the cases: (a) $C_{\mathrm{PFC}} = 50$ μF and (b) $C_{\mathrm{PFC}} = 3$ μF. In agreement with the above analysis, the multiple-parallel system is more robust when the PFC capacitor is 50 μF due to the voltage support at the PCC. Unfortunately, the system turns to be unstable when the PFC capacitor is equal to 3 μF. The analysis reveals that the value of the PFC capacitance has a great impact on the stability of the multiple-inverter systems.

VI. Experimental Verification

For the experimental verification, a laboratory-scale three-inverter prototype with *LCL*-filters is built up to verify the analysis. Its physical layout and parameters are given in Fig. 30 and Table III, respectively. The control scheme is realized with a dSPACE DS1007 platform, whose output PWM signals are channeled through fiber optic cables to commercial inverters. The inverters are then connected to the Chroma 61800 Grid Simulator acting as the ideal grid, while the input dc-link voltages are provided by Yaskawa D1000 regenerative converters. Through the stability analysis in the previous sections, $J_1(s)$ and $J_2(s)$ have different stability regions. According to the root locus analysis, the stable range for $J_1(s)$ is $0 < K_p < 20.1$, whereas the stable range for $J_2(s)$ is $0 < K_p < 27.5$. Note that $J_2(s)$ has a wider stable region than $J_1(s)$. It means that there are four possible combinations for the stable conditions of these two currents:

1) both the self-current and mutual-current are stable;
2) the self-current is stable, but the mutual-current is unstable;
3) the mutual-current is stable, but the self-current is unstable;
4) neither the self-current nor the mutual-current are stable.

The experiment results verify these possibilities. In experiment #1, if the proportional gain K_p satisfies the $J_1(s)$ stable requirement $0 < K_p < 20.1$ ($K_p = 18$ in this case), it certainly meets the $J_2(s)$ stable requirement $0 < K_p < 27.5$. Then, all the three parallel inverters are stable, as shown in Fig. 31. The waveform of the PCC voltage is also stable. For experimental #2, K_p of the 1# and 2# inverter is changed from 18 to 25, and K_p of the 3# inverter is kept the same. In this situation, the mutual-current is unstable while the self-current is stable. It can be observed from Fig. 32 that the resonant current between the 1# inverter and 2# inverter is triggered. Although the 1# inverter and 2# inverter do not work in a proper way, the PCC voltage remains stable and the 3# inverter is also in a stable operation. In experiment #3, K_p values of all three inverters are set above the stable limit 27.5. Then, the results are presented in Fig. 33, where all the three grid currents are unstable. The system stability, which is divided into self-current stability and mutual-current stability, is demonstrated and validated through three experiments.

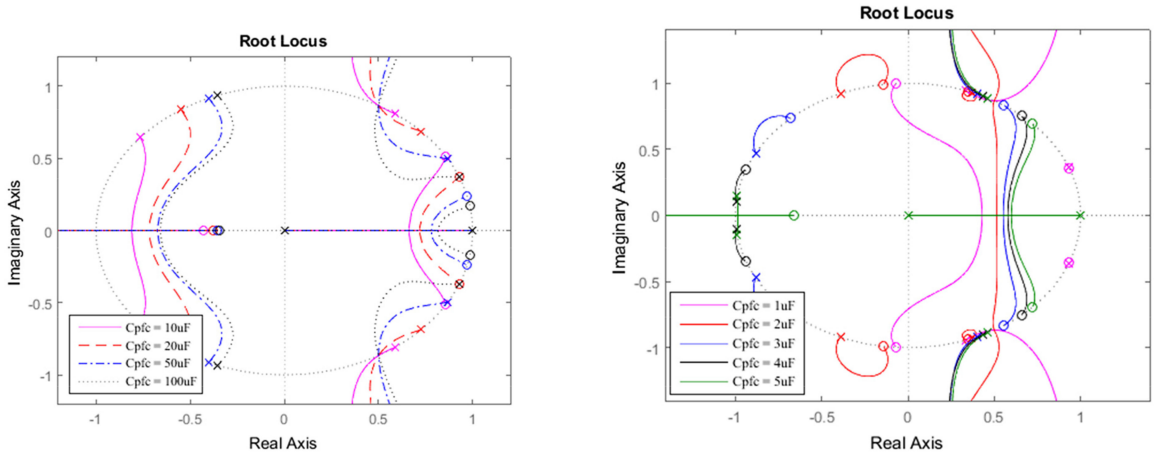

Fig. 28. Root loci for different PFC capacitances. (a) $C_{\mathrm{PFC}} = 10, 20, 50, 100\ \mu$F. (b) C_{PFC} values 1, 2, 3, 4, 5 μF.

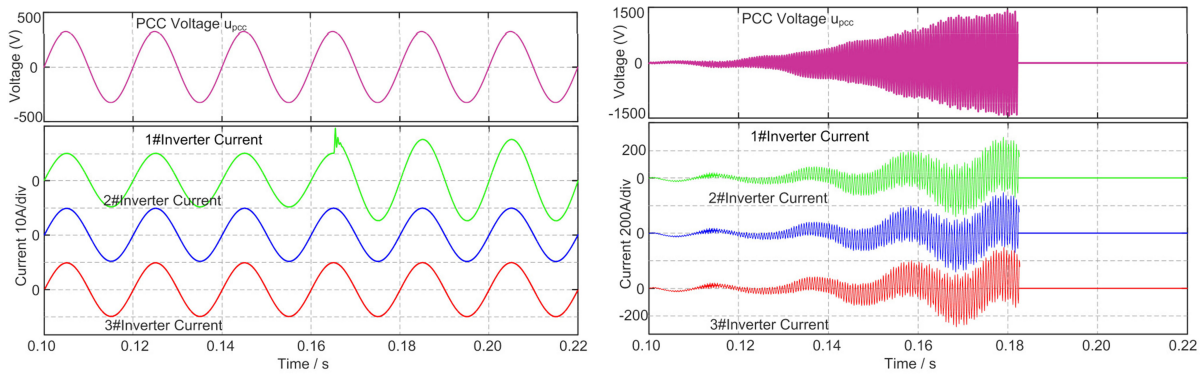

Fig. 29. Simulation results of the system with: (a) $C_{\mathrm{PFC}} = 50\ \mu$F and (b) $C_{\mathrm{PFC}} = 3\ \mu$F.

TABLE II
DIFFERENT GRID CONDITIONS

No.	Grid Inductance L_{g}	SCR
#1	L_{g} = 0 mH	Infinity
#2	L_{g} = 1.7 mH	10
#3	L_{g} = 3.4 mH	5
#4	L_{g} = 8.5 mH	2

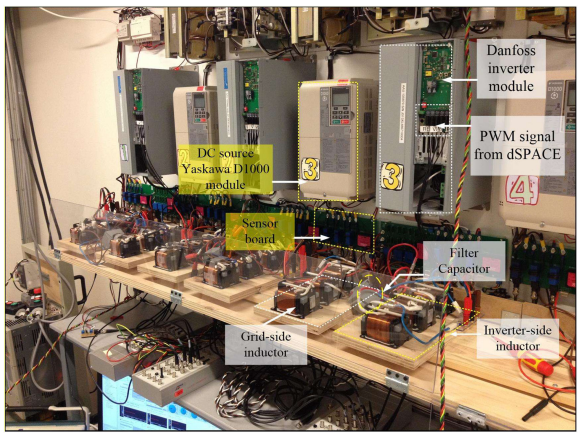

Fig. 30. Laboratory-scale three-inverters prototype, inverter number $n = 3$.

TABLE III
SYSTEM PARAMETERS

Nominal System Parameters		
Converter-side inductor	L_1	1.5 mH
Filter capacitor	C_f	4.7 μF
Grid-side inductor	L_2	1.5 mH
Grid inductance	L_g	1 mH
DC voltage	V_{dc}	730

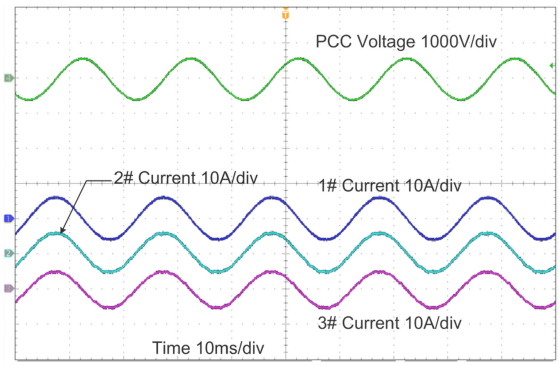

Fig. 31. Both the self-current and mutual-current are stable.

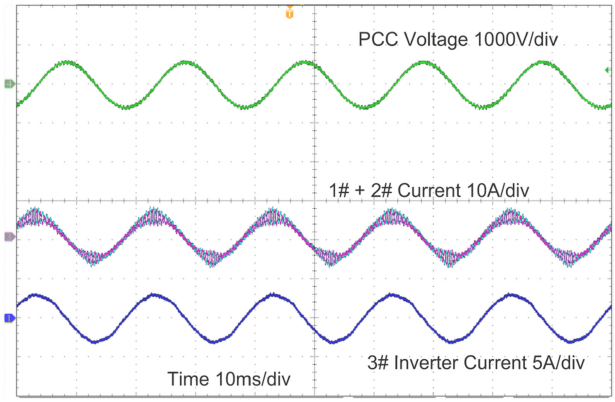

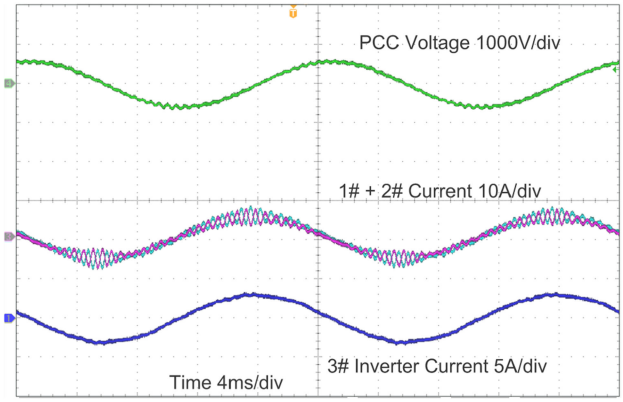

Fig. 32. Mutual-current is unstable, the self-current is stable.

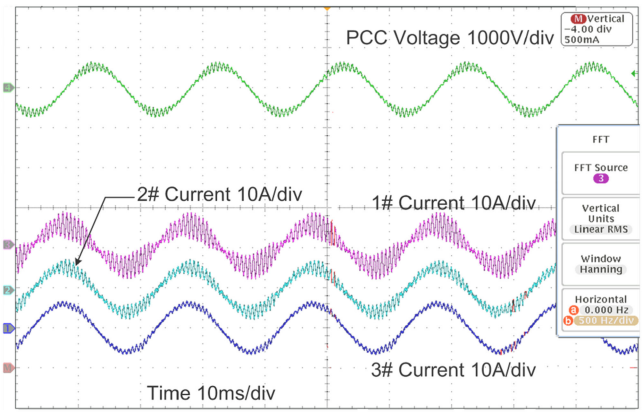

Fig. 33. Mutual-current is unstable, the self-current is unstable.

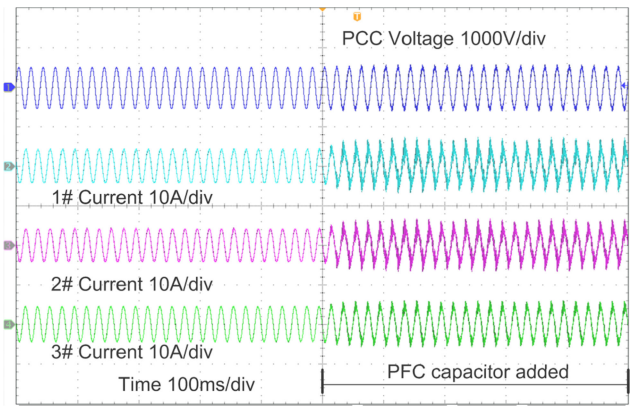

Fig. 34. Experimental test with PFC capacitor $C_{\mathrm{PFC}} = 5\ \mu$F.

To verify the impact of PFC capacitor on the system stability, a three-phase capacitor is inserted in parallel at the PCC. As demonstrated in Fig. 28, different PFC capacitance values will result in different root loci and stability status. It is revealed that a small capacitor will bring unstable poles, leading to system instability. Fig. 34 shows the experimental results with the PFC capacitor equals to 5 μF, the system turns from stable operation to resonant situation. With the increasing PFC capacitor, Fig. 28(a) shows that system will have wider stability range and larger control gain limit because a large capacitor has the function of supporting voltage at PCC point, making the system more robust. Then, 40 μF PFC capacitor is added to the system to replace the 5 μF capacitor. It can be seen from Fig. 35 that an additional capacitor stabilizes a system which is unstable at the beginning point. By adding the capacitor, the system has a better stability status. This is in good agreement with what have been discussed in simulation part.

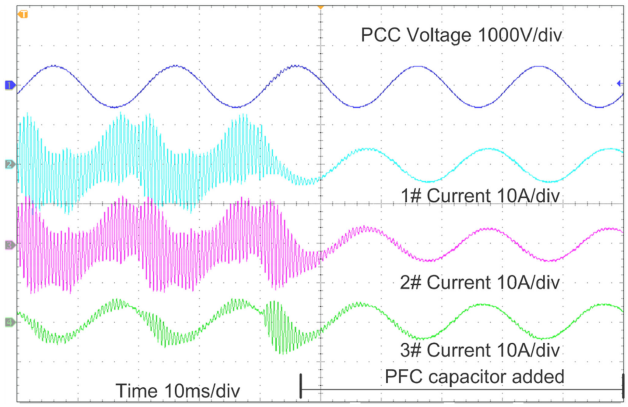

Fig. 35. Experimental test with PFC capacitor $C_{\mathrm{PFC}} = 40\ \mu$F.

VII. Conclusion

This paper investigated the mutual interaction and stability issues of multiple grid-interfacing inverters with *LCL*-filters operating in the power-inverters-based power system in different grid conditions. Such interactions between power inverters and grid will excite multiple resonances at various frequencies under various grid conditions. The *nodal admittance matrix* concept has been adopted in this paper. This paper then developed an *Interaction-Admittance* to describe and model these mutual interactions and coupling effects using a network physical admittance. Different grid scenarios, including the stiff grid condition, the inductive grid condition with/without PFC capacitors, can be well illustrated and analyzed using the proposed model. This model exhibits more intuitive and clearer illustration on multi-inverters system resonance and instability problems, which have been validated through simulations and experiments on a lab-scale prototype.

REFERENCES

[1] B. Kroposki *et al.*, "Achieving a 100% renewable grid: Operating electric power systems with extremely high levels of variable renewable energy," *IEEE Power Energy Mag*., vol. 15, no. 2, pp. 61–73, Mar./Apr. 2017.

[2] F. Blaabjerg, Y. Yang, D. Yang, and X. Wang, "Distributed power-generation systems and protection," *Proc. IEEE*, vol. 105, no. 7, pp. 1311–1331, Jul. 2017.

[3] Renewables 2018: Global Status Report. [Online]. Available: http://www.ren21.net/wp-content/uploads/2018/06/17-8652_GSR2018_FullReport_web_final_.pdf. Accessed on: Jun. 2018.

[4] Danish Energy Agency. Overview Map of the Danish Power Infrastructure in 1985 and 2015. [Online]. Available: https://ens.dk/sites/ens.dk/files/Statistik/foer_efter_uk.pdf. Accessed on: Mar. 6, 2017.

[5] DAMVAD & Kariros Future. DK2050: Green Growth in Denmark Towards 2050—Four Future Scenarios. Mar. 6, 2017. [Online]. Available: http://www.dac.dk/media/54231/Damvad_english_1007.pdf

[6] The official website of Denmark, "A world-leader in wind energy." [Online]. Available: http://denmark.dk/en/green-living/wind-energy/. Accessed on: 2018.

[7] Z. Zou, G. Buticchi, and M. Liserre, "Analysis and stabilization of a smart transformer-fed grid," *IEEE Trans. Ind. Electron.*, vol. 65, no. 2, pp. 1325–1335, Feb. 2018.

[8] M. Lu, X. Wang, P. C. Loh, and F. Blaabjerg, "Resonance interaction of multi-parallel grid-connected inverters with LCL-filter," *IEEE Trans. Power Electron.*, vol. 32, no. 2, pp. 894–899, Feb. 2017.

[9] J. H. R. Enslin and P. J. M. Heskes, "Harmonic interaction between a large number of distributed power inverters and the distribution network," *IEEE Trans. Power Electron.*, vol. 19, no. 6, pp. 1586–1593, Nov. 2004.

[10] F. Blaabjerg and K. Ma, "Wind energy systems," *Proc. IEEE*, vol. 105, no. 11, pp. 2116–2131, Nov. 2017.

[11] J. Agorreta, M. Borrega, J. Lopez, and L. Marroyo, "Modeling and control of N-paralleled grid-connected inverters with *LCL* filters coupled due to grid impedance in PV plants," *IEEE Trans. Power Electron.*, vol. 26, no. 3, pp. 770–1194, Mar. 2011.

[12] C. Zheng, Q. Li, L. Zhou, B. Li, and M. Mao, "The interaction stability analysis of a multi-inverter system containing different types of inverters," *Energies*, vol. 11, no. 9, Aug. 2018, Art. no. 2244.

[13] C. Yu *et al.*, "Modeling and resonance analysis of multi-parallel inverters system under asynchronous carriers conditions," *IEEE Trans. Power Electron.*, vol. 32, no. 4, pp. 3192–3205, Aug. 2017.

[14] D. Yang, X. Wang, and F. Blaabjerg, "Sideband harmonic instability of paralleled inverters with asynchronous carriers," *IEEE Trans. Power Electron.*, vol. 33, no. 6, pp. 4571–4577, Jun. 2018.

[15] R. D. Middlebrook, "Input filter considerations in design and application of switching regulators," in *Proc. IEEE Ind. Appl. Soc. Annu. Meeting*, Oct. 1976, pp. 366–382.

[16] J. He, Y. Li, and D. Bosnjak, "Investigation and active damping of multiple resonances in a parallel-inverter-based microgrid," *IEEE Trans. Power Electron.*, vol. 28, no. 1, pp. 234–246, Jan. 2013.

[17] L. Jia, X. Ruan, Z. Lin, and X. Wang, "An adaptive active damper for improving the stability of grid-connected inverters under weak grid," *IEEE Trans. Power Electron.*, vol. 33, no. 11, pp. 9561–9574, Nov. 2018.

[18] H. K. Khalil, *Nonlinear System*, 3rd ed. Englewood Cliffs, NJ, USA: Prentice-Hall, 2002.

[19] L. Harnefors, A. G. Yepes, A. Vidal, and J. D. Gandoy, "Passivity-based controller design of grid-connected VSCs for prevention of electrical resonance instability," *IEEE Trans. Ind. Electron.*, vol. 62, no. 2, pp. 702–710, Feb. 2015.

[20] C. Yoon, H. Bai, R. Beres, X. Wang, and F. Blaabjerg, "Harmonic stability assessment for multi-paralleled, grid-connected inverters," *IEEE Trans. Sustain. Energy*, vol. 18, no. 3, pp. 888–895, May 2016.

[21] H. Bai, X. Wang, and F. Blaabjerg, "Passivity enhancement in renewable energy source based power plant with paralleled grid-connected VSIs," *IEEE Trans. Ind. Appl.*, vol. 53, no. 4, pp. 3793–3802, Jul./Aug. 2017.

[22] Y. Wang, X. Wang, F. Blaabjerg, and Z. Chen, "Small-signal stability analysis of inverter-fed power systems using component connection method," *IEEE Trans. Smart Grid*, vol. 9, no. 5, pp. 5301–5310, Sep. 2018.

[23] P. Kundur, *Power System Stability and Control*. New York, NY, USA: McGraw-Hill, 1994.

[24] G. John. *Power System Analysis*. New York, NY, USA: McGraw-Hill, 1994.

[25] M. Lu, X. Wang, P. C. Loh, and F. Blaabjerg, "Interaction and aggregated modeling of multiple paralleled inverters with *LCL* filter," in *Proc. IEEE Energy Convers. Congr. Expo.*, 2015, pp. 1954–1959.

[26] D. Pan, X. Ruan, C. Bao, W. Li, and X. Wang, "Optimized controller design for LCL-type grid-connected inverter to achieve high robustness against grid-impedance variation," *IEEE Trans. Ind. Electron.*, vol. 62, no. 3, pp. 1537–1547, Mar. 2015.

[27] M. Liserre, F. Blaabjerg, and S. Hansen, "Design and control of an LCL filter-based three-phase active rectifier," *IEEE Trans. Ind. Appl.*, vol. 41, no. 5, pp. 1281–1291, Sep./Oct. 2005.

[28] S. G. Parker, B. P. McGrath, and D. G. Holmes, "Regions of active damping control for LCL filters," *IEEE Trans. Ind. Appl.*, vol. 50, no. 1, pp. 424–432, Jan./Feb. 2014.

[29] M. Lu, X. Wang, P. C. Loh, F. Blaabjerg, and T. Dragicevic, "Graphical evaluation of time-delay compensation techniques for digitally controlled converters," *IEEE Trans. Power Electron.*, vol. 33, no. 3, pp. 2601–2614, Mar. 2018.

[30] M. Lu, A. Al-Durra, S. M. Muyeen, S. Leng, P. C. Loh, and F. Blaabjerg, "Benchmarking of stability and robustness against grid impedance variation for LCL-filtered grid-interfacing inverters," *IEEE Trans. Power Electron.*, vol. 33, no. 10, pp. 9033–9046, Oct. 2018.

[31] M. Liserre, R. Teodorescu, and F. Blaabjerg, "Stability of photovoltaic and wind turbine grid-connected inverters for a large set of grid impedance values," *IEEE Trans. Power Electron.*, vol. 21, no. 1, pp. 263–272, Jan. 2006.

[32] S. Skogestad and I. Postlethwaite, *Multivariable Feedback Control: Analysis and Design*. New York, NY, USA: Wiley, 1997.

[33] F. Cavazzana, P. Mattavelli, M. Corradin, and I. Toigo, "Grid sensitivity considerations on multiple parallel inverters systems," in *Proc. IEEE 8th Int. Conf. Power Electron. Motion Control*, May 2016, pp. 993–999.

[34] J. R. Massing, G. G. Koch, and A. T. Pereira, "Modeling and stability analysis of current controllers for multi-paralleled grid-connected converters with LCL-filter," in *Proc. IEEE 18th Workshop Control Model. Power Electron.*, Stanford, CA, USA, pp. 1–7, 2017.

[35] M. Lu, X. Wang, P.C. Loh, and F. Blaabjerg, "An analysis method for harmonic resonance and stability of multi-paralleled *LCL*-filtered inverters," in *Proc. IEEE 6th Int. Symp. Power Electron. Distrib. Gener. Syst.*, Aachen, Germany, pp. 1–6, 2015.

[36] X. Chen, Y. Zhang, S. Wang, J. Chen, and C. Gong, "Impedance-phased dynamic control method for grid-connected inverters in a weak grid," *IEEE Trans. Power Electron.*, vol. 32, no. 1, pp. 274–283, Jan. 2017.

Minghui Lu (S'14–M'17) received the B.S. degree from the Harbin Institute of Technology, Harbin, China, in 2011, and the M.S. degree from the Huazhong University of Science and Technology, Wuhan, China, in 2014, both in electrical engineering. He received the Ph.D. degree in power electronics system from Aalborg University, Aalborg, Denmark, in 2017.

He worked with State Grid as an Intern Engineer on the Power Conditioning System for Battery Energy Storage System in 2014. He is a Postdoctoral Researcher with the Department of Electrical Engineering, University of Washington, Seattle, WA, USA. His current research expertise focuses on renewable energy generation, grid-connected converters, control of power electronics converters, and virtual oscillator control in the microgrid application. He has published several top-level journals and conference papers on these areas.

Yongheng Yang (S'12–M'15–SM'17) received the B.Eng. degree in electrical engineering and automation from Northwestern Polytechnical University, Shaanxi, China, in 2009, and the Ph.D. degree in electrical engineering from Aalborg University, Aalborg, Denmark, in 2014.

From 2009 to 2011, he was a postgraduate student with Southeast University, China. In 2013, he spent three months as a Visiting Scholar with Texas A&M University, USA. He is currently an Associate Professor with the Department of Energy Technology, Aalborg University. His research focuses on the grid integration of renewable energy, in particular, photovoltaic, power converter design, analysis and control, and reliability in power electronics.

Dr. Yang is an Associate Editor of the *CPSS Transactions on Power Electronics and Applications* and the *Electronics Letters*. He was the recipient of the 2018 *IET Renewable Power Generation* Premium Award.

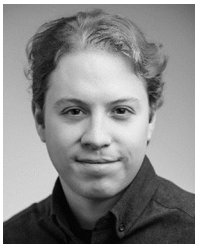

Brian Johnson (S'08–M'13) received the M.S. and Ph.D. degrees in electrical and computer engineering from the University of Illinois at Urbana-Champaign, Urbana, IL, USA, in 2010 and 2013, respectively.

He is the Washington Research Foundation Innovation Assistant Professor within the Department of Electrical and Computer Engineering, University of Washington, Seattle, WA, USA. Prior to joining the University of Washington in 2018, he was an Engineer with the National Renewable Energy Laboratory, Golden, CO. His research interests include renewable energy systems, power electronics, and control systems.

Dr. Johnson was the recipient of the National Science Foundation Graduate Research Fellowship in 2010, and currently serves as an Associate Editor for the IEEE TRANSACTIONS ON ENERGY CONVERSION.

Frede Blaabjerg (S'86–M'88–SM'97–F'03) received the Ph.D. degree in electrical engineering from Aalborg University, Aalborg, Denmark, in 1995.

From 1987 to 1988, he was with ABB-Scandia, Randers, Denmark. He became an Assistant Professor in 1992, an Associate Professor in 1996, and a Full Professor of power electronics and drives in 1998. In 2017, he became a Villum Investigator. He is an Honoris Causa with the University Politehnica Timisoara, Timişoara, Romania, and with Tallinn Technical University, Tallinn, Estonia. He has authored or coauthored more than 600 journal papers in the fields of power electronics and its applications. He has coauthored four monographs and was the Editor of ten books in power electronics and its applications. His current research interests include power electronics and its applications, such as in wind turbines, PV systems, reliability, harmonics, and adjustable speed drives.

He was the recipient of 28 IEEE Prize Paper Awards, the IEEE PELS Distinguished Service Award in 2009, the EPE-PEMC Council Award in 2010, the IEEE William E. Newell Power Electronics Award 2014, and the Villum Kann Rasmussen Research Award 2014. He was the Editor-in-Chief of the IEEE TRANSACTIONS ON POWER ELECTRONICS from 2006 to 2012. He has been Distinguished Lecturer for the IEEE Power Electronics Society from 2005 to 2007 and for the IEEE Industry Applications Society from 2010 to 2011 as well as from 2017 to 2018. Currently he is the President Elect of IEEE Power Electronics Society. He serves as the Vice-President of the Danish Academy of Technical Sciences. He was nominated in 2014, 2015, 2016, and 2017 by Thomson Reuters to be the 250 most cited researchers in engineering in the world.